Full length article

An ultrastructural 3D reconstruction method for observing the arrangement of collagen fibrils and proteoglycans in the human aortic wall under mechanical load

Anna Pukaluk [a,g], Anna-Sophie Wittgenstein [a,1], Gerd Leitinger [b,c,g], Dagmar Kolb [b,c,g], Dominique Pernitsch [c], Sarah A. Schneider [a,h], Patrick Knöbelreiter [d], Verena Horak [e,g], Kristian Bredies [e,g], Gerhard A. Holzapfel [a,f,g], Thomas Pock [d,g], Gerhard Sommer [a,g,*]

[a] Institute of Biomechanics, Graz University of Technology, Graz, Austria
[b] Division of Cell Biology, Histology and Embryology, Gottfried Schatz Research Center, Medical University of Graz, Graz, Austria
[c] Core Facility Ultrastructure Analysis, Center for Medical Research, Medical University of Graz, Graz, Austria
[d] Institute of Computer Graphics and Vision, Graz University of Technology, Graz, Austria
[e] Institute of Mathematics and Scientific Computing, University of Graz, Graz, Austria
[f] Department of Structural Engineering, NTNU, Trondheim, Norway
[g] BioTechMed-Graz, Austria
[h] High-Performance Vision Systems, Center for Vision, Automation and Control, Austrian Institute of Technology, Vienna, Austria, and Human-Robot Interaction Lab, Tufts University, Medford, USA

ARTICLE INFO

ABSTRACT

An insight into changes of soft biological tissue ultrastructures under loading conditions is essential to understand their response to mechanical stimuli. Therefore, this study offers an approach to investigate the arrangement of collagen fibrils and proteoglycans (PGs), which are located within the mechanically loaded aortic wall. The human aortic samples were either fixed directly with glutaraldehyde in the load-free state or subjected to a planar biaxial extension test prior to fixation. The aortic ultrastructure was recorded using electron tomography. Collagen fibrils and PGs were segmented using convolutional neural networks, particularly the ESPNet model. The 3D ultrastructural reconstructions revealed a complex organization of collagen fibrils and PGs. In particular, we observed that not all PGs are attached to the collagen fibrils, but some fill the spaces between the fibrils with a clear distance to the collagen. The complex organization cannot be fully captured or can be severely misinterpreted in 2D. The approach developed opens up practical possibilities, including the quantification of the spatial relationship between collagen fibrils and PGs as a function of the mechanical load. Such quantification can also be used to compare tissues under different conditions, e.g., healthy and diseased, to improve or develop new material models.

Statement of significance

The developed approach enables the 3D reconstruction of collagen fibrils and proteoglycans as they are embedded in the loaded human aortic wall. This methodological pipeline comprises the knowledge of arterial mechanics, imaging with transmission electron microscopy and electron tomography, segmentation of 3D image data sets with convolutional neural networks and finally offers a unique insight into the ultrastructural changes in the aortic tissue caused by mechanical stimuli.

---

* Corresponding author at: Institute of Biomechanics, Graz University of Technology, Graz, Austria.
*E-mail address:* sommer@tugraz.at (G. Sommer).

[1] School of Biomedical Engineering and Imaging Sciences, King's College London, London, UK.

1. Introduction

One of the biggest challenges in vascular biomechanics is to predict the mechanical response of the aorta under (patho)physiological loading conditions. Current advanced mathematical models [1,2] allow the mechanical behavior of the aortic tissue to be reproduced, but further experimental investigations are necessary to find out what drives this behavior [3]. Numerous studies have been carried out with a focus on the human or animal arterial microstructure in order to look for correlations of the mechanical properties with tissue content [4,5] and structure, including, e.g., collagen fiber orientation [6,7] or waviness [8,9]. Nonetheless, none of these parameters alone allow a prediction of aortic tissue mechanics or possible failure.

The composition of the aortic wall is not trivial. Three layers, i.e. intima, media, and adventitia are characterized by distinct mechanical properties and architecture [10]. It was shown that the strength of the aorta is maintained mainly by the components of the extracellular matrix (ECM) [10], in particular by collagen [11]. Specifically, earlier studies showed that the aortic wall mainly accommodates collagen molecules of type I and III [12–14], which form collagen fibrils [15–17]. Some studies focused on the mechanical characterization of an isolated collagen monomer [18] or fibril [19], but it should be taken into account that collagen fibrils do not act independently in the aortic wall [20]. Recent studies have shown that bundles of collagen fibrils, i.e. collagen fibers, change their microstructural organization in loaded arterial tissues [21–25]. Nevertheless, the mechanical properties of the tissue may not only be limited to the micro-architecture, but also be influenced by the quality [26] and integrity [27] of the collagen fibers.

The collagen fiber, visualized with electron microscopy, e.g., by Dingemans et al. [28], can be described as a bundle of collagen fibrils with interposed proteoglycans. Proteoglycans (PGs) are molecules that consist of a core protein with one or more covalently attached glycosaminoglycan chains [29,30]. It should be noted that different types of PGs in the aorta have been identified either directly in the ECM or in collagen fibers. The main PG is versican, which is located in the medial and endothelial layers, while small leucine-rich PGs such as decorin and biglycan are often found incorporated in collagen fibers [31,32]. PGs have drawn attention in current studies on the aorta [33] and it has been shown that their content increases significantly in diseases of the aortic wall such as atherosclerosis [34,35] or aneurysm formation [36]. Note that the mechanical behavior of healthy to diseased arterial tissues also changes [37,38], although the mechanical role of PGs in the altered arterial mechanics has not yet been shown. The mechanical role of PGs in collagen fibers embedded in soft tissues is the subject of ongoing debate [39]. The proposed hypotheses that are assigned to PGs range from roles of load-transmitting elastic bridges between collagen fibrils [40,41], mechanical couplings [42], assistance for sliding [39,43], to eventually no load-transmission role, but an influence on the stress relaxation [44]. In addition, it was suggested that the osmolarity of the interstitial fluid determines the mechanical properties of PGs, which consequently change the stretching and folding patterns of collagen fibers [45] and the mechanical response of the tissue [46]. The mechanical role of PGs in arterial collagen has hardly been studied. However, some studies have focused on the general presence of PGs in arteries and their relationship to the mechanics of the aorta. Azeloglu et al. [47] suggested that PGs maintain residual stresses in the aortic wall, while Mattson et al. [48] suggested that PGs, or more precisely glycosaminoglycans, could play an important role in collagen recruitment. In summary, the possibility of the mechanical role of PGs in soft tissues, including arteries, should not be rashly denied, as the glycan molecule can be stretched up to 10% [49] and
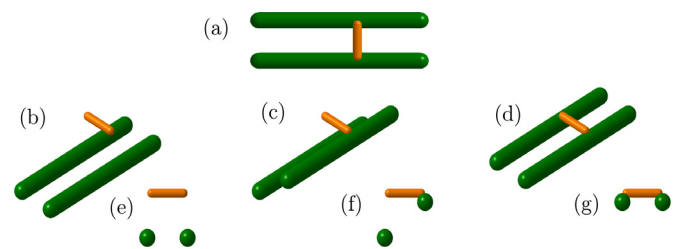
Fig. 1. Illustration of alternative interpretations of geometric 3D structures when imaged in 2D. Exemplary objects shown in-plane (a) are followed by three possible 3D arrangements shown in (b),(e), then (c),(f), and (d),(g) as axonometric projections are shown in (b)–(d) and side views in (e)–(g).

the binding force between a collagen fibril and a PG is estimated to be greater than the strength of a glycosaminoglycan chain [42].

The aim of this study is therefore to advance our knowledge of the ultrastructure of collagen fibers embedded in the human aortic wall that is exposed to biaxial mechanical loads in planar configuration. We stretched the aortic wall equibiaxially and used electron tomography [50], an advanced technique of transmission electron microscopy (TEM) [51,52], to record the three-dimensional (3D) organization of collagen fibrils and PGs. The 3D organization was then reconstructed using different segmentation approaches. It should be emphasized that a 3D investigation technique has distinct advantages over a 2D investigation technique which only provides 2D projections of fairly complex 3D structures. The lack of the third dimension can lead to a serious misinterpretation of the geometry and arrangement of the depicted objects, as shown in Fig. 1.

2. Methods

The protocols for sample preparation, biaxial extension test, transmission electron microscopy, volume reconstruction, and segmentation of collagen fibrils and PGs were performed on specimens obtained from a non-atherosclerotic and non-aneurysmal 56-year-old male human abdominal aorta. The aorta was received within 24 hours after death and stored in phosphate-buffered saline (PBS), pH 7.4, and at 4°C until testing, which was completed within 24 hours after specimen delivery. The use of autopsy material has been approved by the local Ethics Committee of the Medical University of Graz (27-250 ex 14/15).

2.1. Sample preparation for mechanical testing

The intact aortic tube was cut open longitudinally and three square samples measuring 20×20 mm and one rectangular sample measuring 10×5 mm were cut. The square samples were subjected to biaxial extension tests, while the rectangular sample was fixed directly overnight in the load-free state with 2% glutaraldehyde in PBS at 4°C prior to preparation for electron microscopy. Particular care was taken to ensure that edges of the square and rectangular samples were in line with the circumferential and longitudinal directions of the aorta. The mean thickness of each sample was measured optically according to the method described in Sommer et al. [53].

For biaxial testing, each square sample was pierced with four sets of five hooks connected with surgical sutures [54]. In order to ensure reproducible results and a uniform strain field in the middle of the sample during the test, the template was designed for hooking based on the findings of Eilaghi et al. [55]. The distance of 3 mm between the hooks on each side together with the distance of 2 mm between the specimen edge and the hooks resulted in the smallest practical distance between the attachment points on adjacent edges (Fig. 2(a)). The surface of the sample was sprinkled
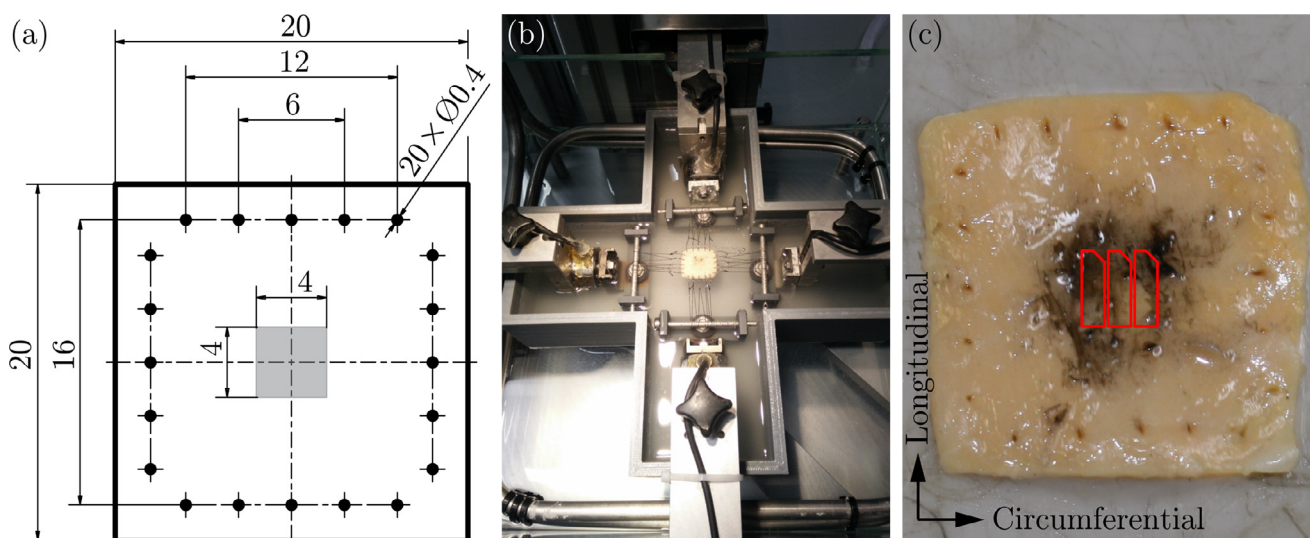
Fig. 2. (a) Hooking template based on the results of Eilaghi et al. [55] with an area in the middle used for optical tracking, marked in gray; (b) specimen that was hooked into the biaxial extension testing device [56] according to the specification and submerged in a basin filled with glutaraldehyde for fixation in the stretched state; (c) sample after fixation shows the luminal side, with red boundaries representing the cutting pattern before sample preparation for electron tomography.

by a black pulverized tissue marker (BioGnost Ltd., Zagreb, Croatia) in order to generate a scattered pattern that is suitable for optical tracking via the video-extensometer (VE) such as [6].

2.2. Biaxial extension testing

The prepared samples were mounted in a biaxial testing device as described by Sommer et al. [56]. In short, the setup integrates four linear actuators with load cells, which are mounted using L-shaped brackets, and a VE system laserXtens (ZwickRoell Testing Systems GmbH, Fürstenfeld, Austria) that enables two-dimensional, non-contact stretch measurements in the center of the sample using a scattered pattern on the sample surface. During the test, the sample is submerged in PBS, which is tempered at 37°C (Fig. 2(b)).

In this study, a stretch-driven protocol based on VE measured stretches was used. The samples were loaded equibiaxially and quasi-statically at a rate of 3 mm/min. Each of the three square samples was tested at a different stretch level, i.e. the first sample up to $\lambda = 1.05$, the second up to 1.10, and the third up to 1.15. The proposed stretch levels are based on the finding of Kamenskiy et al. [57], who showed that the maximum stretch of an abdominal aortic wall during the equibiaxial test could be 1.05. The subsequent 1.10 and 1.15 stretching steps were a natural consequence of the first step. Each sample was subjected to a preload of about 20 mN followed by five cycles of preconditioning to obtain reproducible responses. Thereafter, each sample was reloaded until the maximum stretch level, i.e. $\lambda = 1.05$, 1.10, and 1.15, respectively, and was held at this stretch level. While the specimen was held at its defined stretch level, the PBS in the basin was replaced by 2% glutaraldehyde in PBS and left there for 4 hours at room temperature for thorough sample fixation.

In order to quantify the mechanical behavior of the tissue, Cauchy stresses in the circumferential (θ), and longitudinal (z) directions were calculated according to Humphrey et al. [58]

$$\sigma_{\theta\theta} = \lambda_\theta \frac{f_\theta}{HL_z}, \qquad \sigma_{zz} = \lambda_z \frac{f_z}{HL_\theta}, \qquad (1)$$

where λ_θ and λ_z are the stretch ratios computed on the basis of the VE data sets, f_θ and f_z are the loads measured by the load cells, L_θ and L_z are the undeformed specimen lengths over which

the loads act (all in the circumferential or longitudinal direction), and H is the undeformed thickness obtained by optical measurements. Only normal stresses were calculated, assuming that shear stresses in planar biaxial extension tests on fiber-reinforced material are negligible, as shown by Sommer et al. [56] for the human myocardium and confirmed by Niestrawska et al. [6] for human aortic tissues.

2.3. Sample preparation for transmission electron microscopy

Upon fixation, the center of each sample was cut into three rectangles measuring about 2×5 mm, the longest edge of which indicated the longitudinal direction of the aorta. In order to create a geometry that makes it possible to maintain the orientation and the order of the layers after the sample preparation has been completed, the upper right corner was cut while the tunica intima was on top (Fig. 2(c)). The same procedure was applied to the sample fixed at the load-free state.

The staining and embedding protocols followed that of Williams et al. [59]. In short, post-fixation was carried out overnight in 1% Cupromeronic Blue (Polysciences Europe GmbH, Hirschberg an der Bergstrasse, Germany) in 0.2 M acetate buffer with 0.3 M MgCl$_2$ sought to uncover PGs. Each sample was then rinsed in 0.2 M acetate buffer containing 0.3 M MgCl$_2$. One hour immersion in 0.5% Na$_2$WO$_4$ in acetate buffer followed by an overnight immersion in 0.5% Na$_2$WO$_4$ in 30% ethanol. Next, a rinse in distilled water was performed before staining with 1% uranyl acetate in 0.1 M acetate buffer for one hour to visualize collagen fibrils. The samples were rinsed in 0.1 M maleate buffer and later in distilled water, and dehydration was performed with graded ethanol and propylene oxide. Finally, the specimens were infiltrated and embedded in epoxy resin (TAAB Laboratories Equipment Ltd, Reading, UK) and polymerized at 60°C for 3 days (the reader is referred to [60] for further details).

The embedded samples were trimmed so that the longest edge continuously corresponds to the longitudinal direction of the aorta (see Fig. 3). An EM UC 7 Ultramicrotome (Leica Microsystems, Vienna, Austria) was used to cut semi-thin sections with a thickness of 500 nm with a glass knife, and the sections were stained with toluidine blue (Agar Scientific Ltd, Essex, UK) to identify the aor-
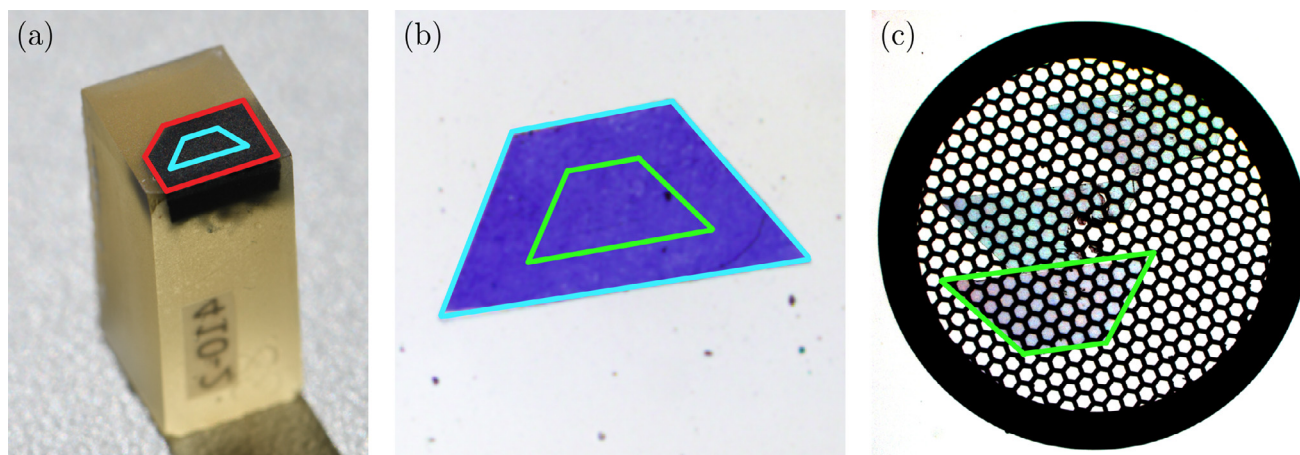
Fig. 3. (a) Representative sample stained and embedded in epoxy resin. The red boundaries represent the geometry section after fixation in the stretched state, see Fig. 2(c). The blue boundaries represent the trimmed edges of a semi-thin section in (b), while the green contour represents the perimeter of the ultra-thin section in (c). The longest edge indicates the longitudinal direction of the aorta.

tic layers. Since toluidine blue is a monochromatic stain, we also tried methylene blue-azure II-basic fuchsin, a polychromatic stain, to help identify the aortic layers. To produce the methylene blue-azure II-basic fuchsin stain, a solution of methylene blue (Bayer-Meister-Lucius, Leverkusen, Germany) and azur II (Fluka Chemie GmbH, Buchs, Switzerland) was first used according to the rapid staining method of Böck [61]. Then 3 ml of the solution of methylene blue-azur II and 2 ml of a base solution of a basic fuchsin (Carl Roth GmbH, Karlsruhe, Germany) were mixed in 3 ml of 0.2 M sodium phosphate buffer (pH 7.4). Images of the stained semi-thin sections were recorded using a transmitted light microscope Leica DM 6000 B (Leica Microsystems, Vienna, Austria).

The 250 nm thick ultra-thin sections for electron tomography were cut with a diamond knife again using an EM UC 7 Ultramicrotome (Leica Microsystems, Vienna, Austria). These sections were contrasted with 2% uranyl acetate in double distilled water for 30 min and lead citrate for 30 s. Finally, protein A coated colloidal 10 nm gold particles (BBI Solutions, Blackwood, UK) were applied to both sides of the grid for 10 min to act as fiducial markers [60,62,63].

2.4. Transmission electron microscopy

Transmission electron micrographs were recorded with a Gatan Ultrascan 1000 charge coupled device (CCD) camera (temperature $-25°C$; acquisition software Digital Micrograph; Gatan, Munich, Germany) on a Tecnai G2 20 transmission electron microscope (TEM) (FEI, Eindhoven, Netherlands) [62,64] at an acceleration voltage of 200 kV in bright-field mode with the help of the software package SerialEM (Mastronarde Group, University of Colorado, Boulder, USA) [65].

When the ultrastructure of the tissue was analyzed, a montage of about 100 images was first recorded over the region of interest (ROI) with a pixel size of 12 nm. The ROI was chosen for the area that contained collagen fibers representative for the specific sample and allowed high tilt angles. Next, the area within the ROI was selected for tomography and exposed to a dose of 2000 e per $Å^2$ to minimize shrinkage and warping of the section during single-axis tilt series captured from $-65°$ to $+65°$ in an angular step of $1°$ with a pixel size of 0.5 nm. The software IMOD (Mastronarde Group, University of Colorado, Boulder, USA) [66] was used to align the tilt series and to reconstruct tomograms using the back projection algorithm. The principle of electron tomography and volume reconstruction is shown schematically in Fig. 4. Finally, the reconstructed tomograms had a size of $2048 \times 2048 \times 100$ cubic voxels

with a voxel edge length of 0.5 nm. The microscopy images and reconstructed tomograms were visualized with the open source software package Fiji [67].
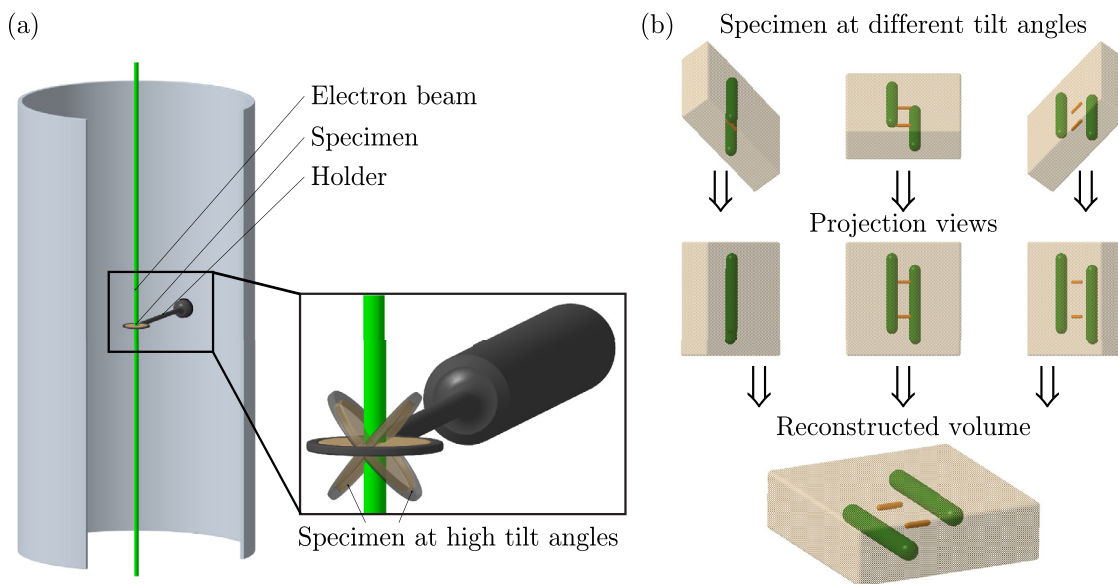
2.5. Segmentation

In this study, several segmentation approaches were examined in order to find a method that effectively separates PGs and collagen fibrils [68]. First, a two-stage method was studied [69]. The first stage of this approach based on a deep-learning approach using a convolutional neural network (CNN) [70,71] for patch-based weak binary image segmentation. In the second stage, a total-variation- and thresholding-based classifier was applied to obtain smooth and regular binary segmentation. In subsequent attempts that are described in detail in the following, preprocessing with TV-ℓ_1 denoising [72] followed directly by binarization with a defined threshold value was considered. Next, a tube detection filter [73] was applied prior to hysteresis thresholding. Finally, the segmentation was carried out again based on a deep learning approach, in particular a CNN using U-Net [74] and ESPNet [75] models.

The TV-ℓ_1 denoising is a total variation based model that is obtained from the Rudin-Osher-Fameti model [76] by replacing the quadratic data fitting term with a ℓ_1 norm data fitting term [72], which leads to

$$\min_u \int_\Omega |Du| + \lambda ||u - f||_1, \tag{2}$$

where Ω is the domain of the image u and the given noisy image f, Du is the distributional derivative of u and λ is the regularization parameter. The TV-ℓ_1 model has the nice property to be contrast invariant, i.e., the regularization parameter λ can be used to tune the maximum size of the structures that are removed during the denoising process invariant to the contrast of these structures. Hence, the interesting but low-contrast structures are not lost during the denoising. The TV-ℓ_1 denoising was applied to reconstructed tomograms in 3D, whereby the resolution was reduced to $512 \times 512 \times 25$ voxels in order to reduce the computation time. The intensities of each preprocessed image $u(x)$ were normalized between 0 and 1 for each pixel x. Eventually, the image $u(x)$ was binarized with a selected threshold value t so that the binarized image $v(x)$ was obtained as

$$v(x) = \begin{cases} 1 & \text{if } u(x) \geq t, \\ 0 & \text{else.} \end{cases} \tag{3}$$

(a)

(b) Specimen at different tilt angles

Electron beam

Specimen

Holder

Specimen at high tilt angles

Projection views

Reconstructed volume

Fig. 4. (a) Schematic representation of a tilt series recording for electron tomography. Transmission electron microscopy images are taken at various tilt angles, starting at the negative high angle through the horizontal position of the sample to the positive high angle. (b) Steps of the electron tomography comprise the recording of projection views of a specimen at different tilt angles and volume reconstruction, e.g., by means of a back projection algorithm from the projection views. Illustration is based on Fig. 1 of Subramaniam et al. [50].

Alternatively, a tube detection filter was used [73]. In short, this filter improves structures with tubular geometry, i.e., structures of circular cross-section in which intensities change similarly to a Gaussian distribution and with fairly constant intensities along the axis. The neighborhood of a pixel x_0 in an image u was examined using the Taylor expansion

$$u(x_0 + \Delta x) \approx u(x_0) + \Delta x \nabla u(x_0) + \frac{1}{2} \Delta x^{\mathrm{T}} \nabla^2 u(x_0) \Delta x, \qquad (4)$$

where $\nabla u(x_0)$ is the gradient vector and $\nabla^2 u(x_0)$ is the Hessian matrix at x_0. Since the tubular structures can appear in different sizes [77], a scale σ was introduced [73]. Therefore,

$$\nabla^2 u^{\sigma}(x_0) = \sigma^2 \nabla^2 u(x_0) \qquad (5)$$

describes the Hessian matrix of pixel x_0 at the scale σ, and u^{σ} is the image u smoothed with a Gaussian filter with standard deviation σ.

Next, the local curvature around the pixel x_0 was analyzed by an eigenvalue decomposition of the scaled Hessian matrix, resulting in three orthonormal directions, v_1, v_2 and v_3 ($|v_i| = 1$), which can also be understood as principal axes. The corresponding eigenvalues λ_1, λ_2 and λ_3 ($|\lambda_1| \leq |\lambda_2| \leq |\lambda_3|$) can be interpreted as moments of inertia about these axes. For a tube, v_1 is in line with the tube axis, the following relations are fulfilled

$$|\lambda_1| \approx 0, \quad |\lambda_1| \ll |\lambda_2|, \quad |\lambda_2| \approx |\lambda_3|, \qquad (6)$$

where λ_1 is very small, ideally zero, λ_2 and λ_3 are greater than λ_1 and similar, ideally equal [73].

Furthermore, Frangi et al. [73] proposed two dissimilarity measures, namely R_B and R_A, and a measure for the 'second-order structureness' S. Consequently,

$$R_B = \frac{|\lambda_1|}{\sqrt{|\lambda_2 \lambda_3|}}, \qquad R_A = \frac{|\lambda_2|}{|\lambda_3|}, \qquad S = \sqrt{\sum_{j \leq n} \lambda_j^2}, \qquad (7)$$

where n is the dimension of the image. The ratio R_B reaches its maximum for a blob-like structure and therefore evaluates the deviation of the given structure from the spherical geometry. The R_A takes into account the aspect ratio of the two largest eigenvalues and thus allows the recognition of tubular structures for

which R_A approaches 1. The measure S complements the regions of high contrast where at least one of the eigenvalues is large. Finally, the tubularity function R for dark structures on a light background states

$$R = \begin{cases} 0 & \text{if } \lambda_2 < 0 \text{ or } \lambda_3 < 0, \\ \left[1 - \exp\left(-\frac{R_A^2}{2\alpha^2}\right)\right] \\ \left[\exp\left(-\frac{R_B^2}{2\beta^2}\right)\right]\left[1 - \exp\left(-\frac{S^2}{2c^2}\right)\right] & \text{else,} \end{cases}$$

$$(8)$$

where α, β, and c are threshold values that regulate the sensitivity of the filter [73]. To further improve the results, hysteresis thresholding was implemented, so a high and a low threshold were chosen. A response above the high threshold was accepted and considered a strong response, while a response below the low threshold was rejected. A response between high and low thresholds was only accepted if it was close to a strong response.

CNNs are widely used deep learning approaches for image analysis-related tasks [70,71]. The distinguishing feature of CNN is that network layers are not fully connected, each neuron is only connected to the neighboring neurons of the next layer. In addition, a set of weights called the kernel is shared for each neuron in the layer. Local connectivity and weight distribution offer advantages through the reduction of parameters, i.e. the ability to handle data with large dimensions. For the two networks described below, i.e. U-Net [74] and ESPNet [75], the following functions have been implemented [68]. The leaky rectified linear unit (LReLU) function

$$f(x) = \begin{cases} \alpha x & \text{if } x \leq 0, \\ x & \text{if } x > 0, \end{cases} \qquad (9)$$

where $\alpha = 0.01$ was used to activate inner layers, whereas the sigmoid function

$$f(x) = \frac{1}{1 + \exp(-x)} \qquad (10)$$

activated the output layer [78]. The cross-entropy loss [79], also called log loss, was used as the loss function. Since only two
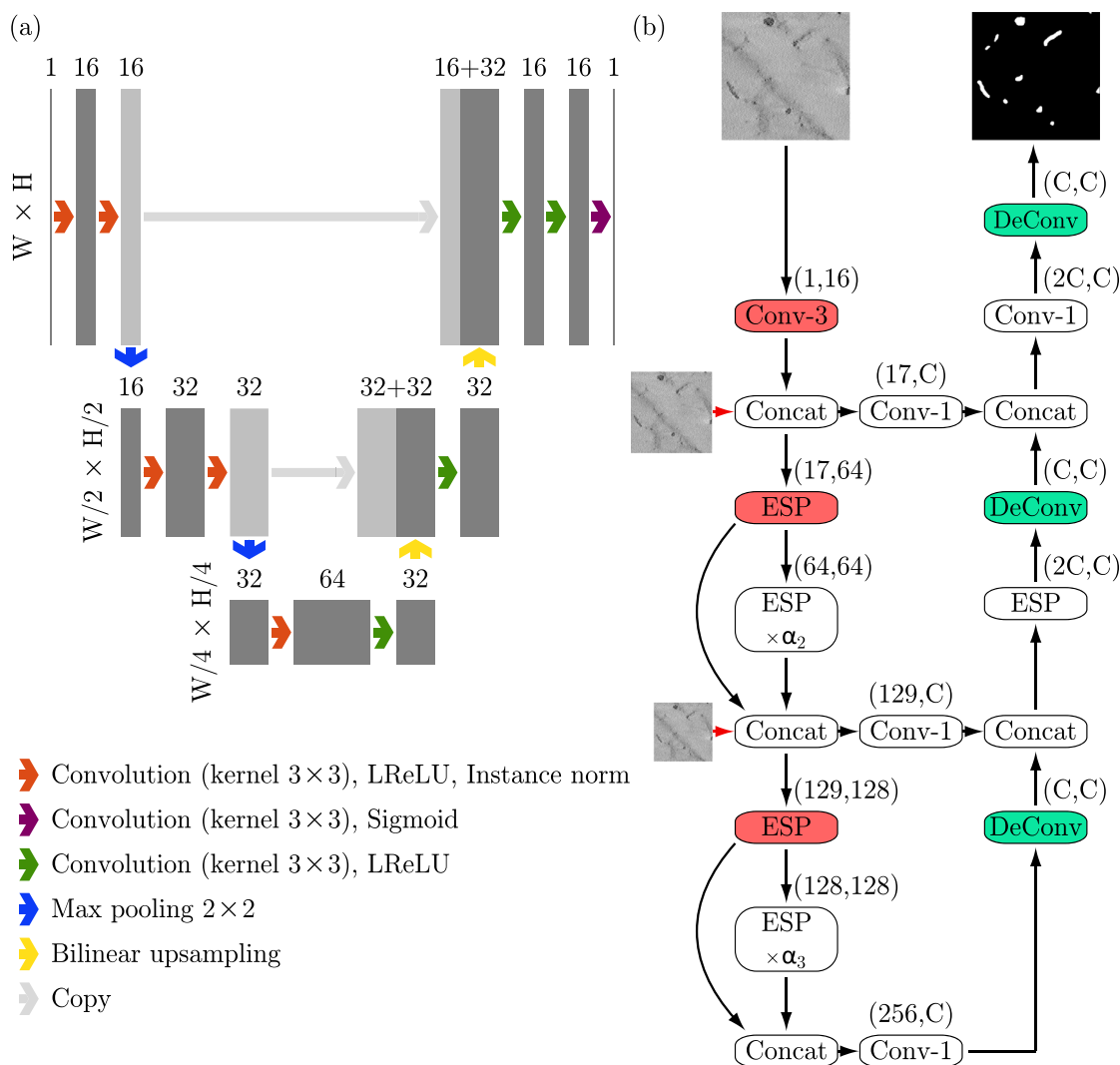
Fig. 5. The architectures of the networks used in this study were based on the U-Net (a), modified from Ronneberger et al. [74], and ESPNet (b), adapted from Mehta et al. [75]. In (a), gray boxes represent feature maps and light gray boxes correspond to the copied feature maps. The number of channels is shown at the top of each box. The resolution for each level is shown on the left as a fraction of the input resolution $W \times H$. In (b), the down- and up-sampling modules are marked red and green, respectively. The following abbreviations for modules are used: Conv-n = convolution with a $n \times n$ kernel; Concat = concatenation; DeConv = deconvolution. The number of input and output channels is noted above the modules, where C represents the number of classes in the data set and corresponds to 1 in our application.

classes are needed for our application, namely proteoglycan and non-proteoglycan or collagen and non-collagen, the binary cross-entropy loss function $\ell_{\mathrm{BCE},x}$ for a pixel x can be expressed as

$$\ell_{\mathrm{BCE},x} = -[t_x \log(\sigma(o_x)) + (1 - t_x)\log(1 - \sigma(o_x))], \tag{11}$$

where t_x is the target and $\sigma(o_x)$ is the probability estimate for the output o_x, all at the pixel x. The final loss value is calculated as the loss averaged over all pixels. To minimize the loss, the adaptive moment estimation (Adam) optimizer was chosen [80,81]. Adam optimizer updates the parameters $\theta \in \mathbb{R}^d$ of the model with the rule
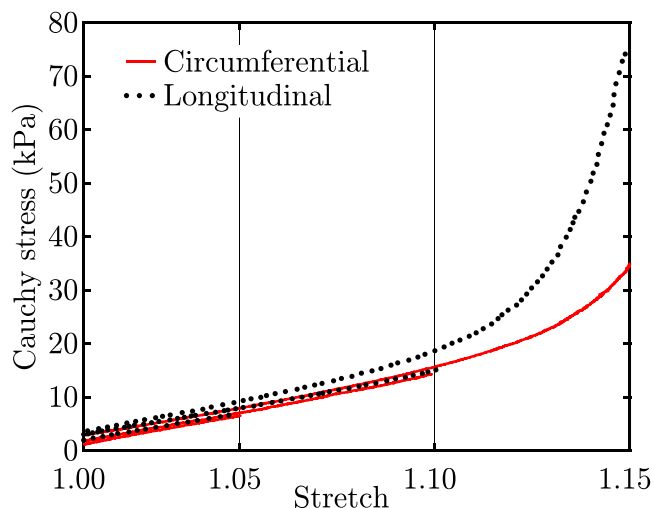
$$\theta_{t+1} = \theta_t - \frac{\tau}{\sqrt{\tilde{v}_t} + \epsilon} \tilde{m}_t, \tag{12}$$

where θ_{t+1} are the updated parameters with respect to the parameters θ_t, taking into account the gradient of the loss function as expressed in the bias-corrected first and second raw moment estimates $\tilde{m}_t$ and $\tilde{v}_t$, respectively, and controlled by the increment τ and the smoothing term ϵ [80]. In addition, the performance of both networks has been significantly improved with the addition of a normalization layer. As a result, the instance normalization

[82] was selected, which could also be viewed as a special case of the group normalization [83].

The first network examined as part of this study was based on the U-Net architecture proposed by Ronneberger et al. [74] with its modification for feature extraction proposed by Knöbelreiter et al. [84], see Fig. 5(a) for the network architecture and [68] for details. In short the network consists of a contracting and an expansive path. In the contracting path, convolutions are followed by an LReLU activation function and an instance normalization, the down-sampling is carried out by the max pooling method. The expansive path consists of convolutions with the LReLU activation function, bilinear up-sampling and the sigmoid activation function on the last layer.

The other network examined followed the efficient spatial pyramid network (ESPNet) approach proposed by Mehta et al. [75], see Fig. 5(b) for the network architecture and [68] for specifications. In short, the ESPNet architecture consists of an encoder and a decoder path. In the encoder path, the down-sampling is implemented by the convolution and ESP modules. The deconvolution is responsible for the up-sampling in the decoder path. At a given level n, the

Fig. 6. Cauchy stress vs. stretch behavior in the circumferential direction (red solid curve) and the longitudinal direction (black dotted curve) of equibiaxially stretched specimens from the human abdominal aorta. The tests were stopped for sample fixation at the stretch of 1.05, 1.10, and 1.15, respectively.

Table 1
Cauchy stresses in circumferential ($\sigma_{\theta\theta}$) and longitudinal (σ_{zz}) directions calculated for the human abdominal aortic wall at 1.05, 1.10, and 1.15 stretch (λ_θ, λ_z) during the equibiaxial test.

$\lambda_\theta, \lambda_z$	$\sigma_{\theta\theta}$ (kPa)	σ_{zz} (kPa)
1.05	7.3	7.1
1.10	15.4	14.5
1.15	75.2	35.5

3. Results

This section is intended to evaluate the procedures proposed in Chapter 2. The results of the planar biaxial extension test, staining of semi-thin sections, the electron tomography and finally the segmentation of collagen fibrils and PGs are presented and analyzed.
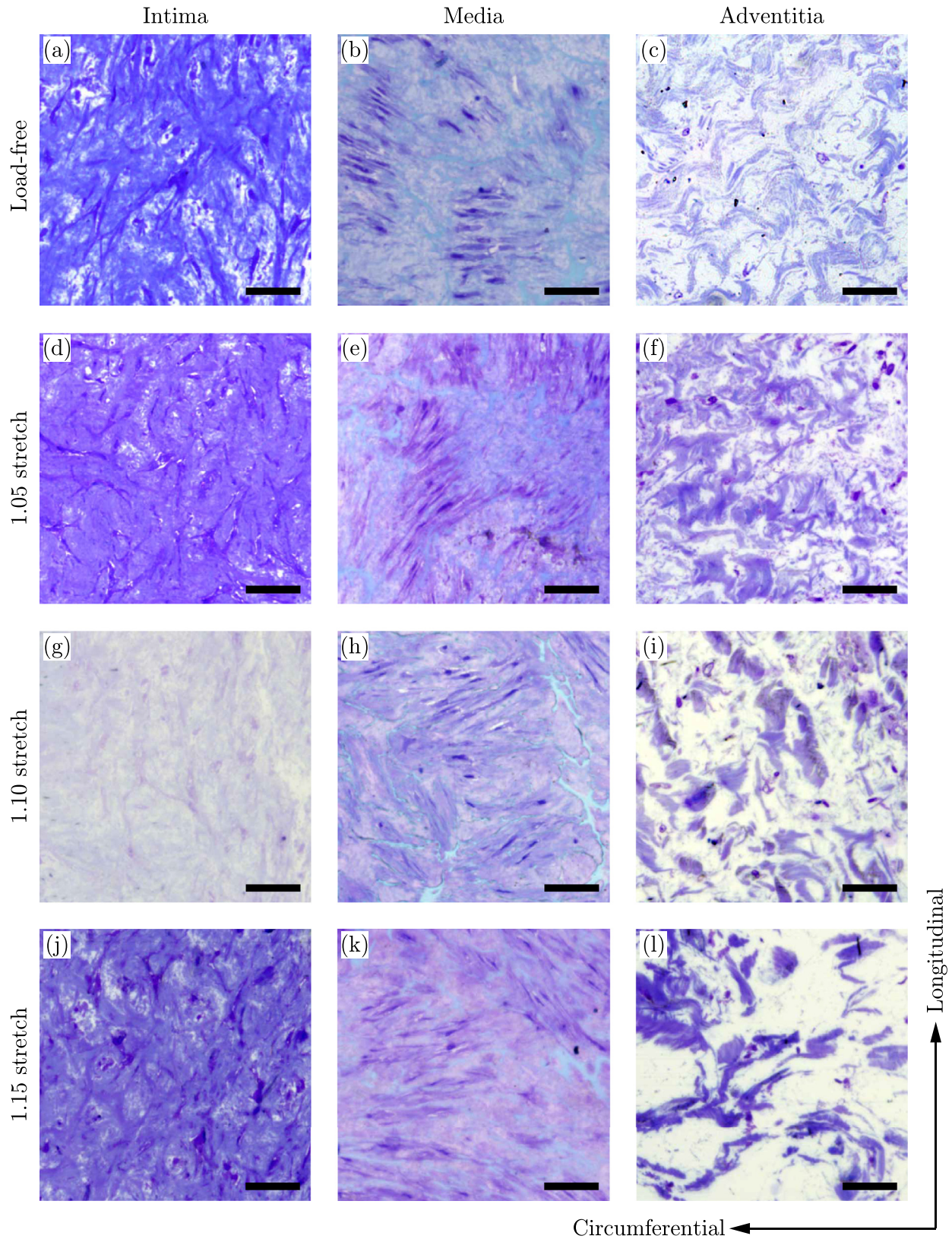
3.1. Biaxial extension test

No apparent damage or rupture of the tissue was observed during the experiments. After five cycles of preconditioning, the stress-stretch curve stabilized and become repeatable as expected based on previous studies [87–89]. Furthermore, the reproducibility of the test results confirmed no impairment of the samples during preparation. It is noteworthy that all of the tissue patches produced remarkably similar mechanical responses within the range of stretch achieved. This could indicate a uniform tissue composition and comparable ultrastructure across all tested samples.

The aortic wall showed anisotropy with a more compliant behavior in the circumferential direction (Fig. 6). A nonlinear mechanical response [90] was also found, although 1.15 was the maximum stretch achieved. The fixation of the samples in the unloaded state and at different stretch levels, i.e. 1.05, 1.10, and 1.15, captured various stages of the aortic wall response to the applied load. At the stretch of 1.05, the stress-stretch behavior was linear, while the stretch of 1.10 corresponded to the end of the linear regime. The stretch of 1.15 was related to tissue stiffening. The stress-stretch responses are shown in Fig. 6, while Cauchy stress values at defined stretch levels are shown in Table 1. The sample fixation with glutaraldehyde in the stretched state was considered as successful, since neither sample shrinking nor other deformations were observed after releasing the load, i.e., removal of the tissue from the testing device.

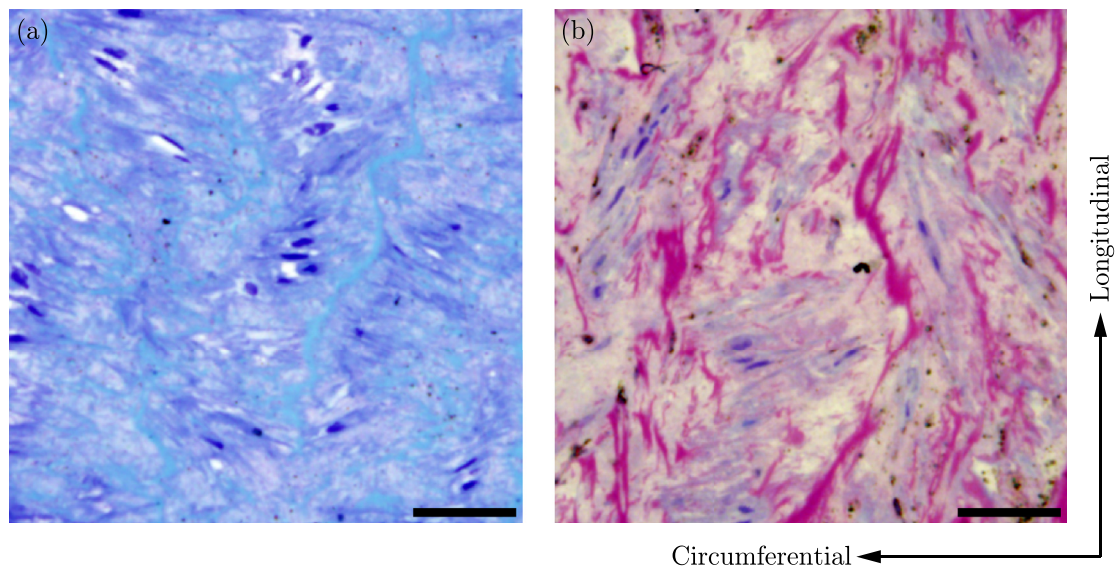### 3.2. Layer identification for transmission electron microscopy

Since we have tested and embedded an intact abdominal aortic wall consisting of specific layers, the staining of semi-thin sections is of great importance in order to ensure the correct layer recognition prior to electron microscopy [60] because the layers cannot be identified with naked eye after Cupromeronic Blue staining. Fig. 7 illustrates the microstructure of the aortic layers at the load-free state and with stretches of 1.05, 1.10, and 1.15 using toluidine blue staining. Since toluidine blue is often used to stain a variety of cells [91,92] and the media mainly consists of vascular smooth muscle cells [28,93], it was used for layer identification. Due to its glycosaminoglycan content, toluidine blue also stains collagen bundles [91,92]. The intima was recognized by a carpet-like architecture of intimal collagen, while the adventitia was identified by diagonally and longitudinally aligned thick collagen bundles [6].

On the medial layer (Fig. 8) the methylene blue-azur II-basic fuchsin staining was tested in order to improve the differentiation of the ECM components, especially of collagen and elastin, as early studies attributed clearly different colors to these proteins [94,95].

ESP module is repeated α_n times, where α is a hyperparameter that controls the depth of the network.

For both networks, the ground truth representing PGs or collagen fibrils was manually segmented by an experienced operator using the software Fiji [67]. Finally, twelve segmented images were divided into eight training and four validation images. In order to reduce the computing time, the resolution of the input and target images has been reduced by two. In addition, the images were divided into four quadrants and the intensities were normalized between 0 and 1. Since the small amount of training data caused severe overfitting, data augmentation was necessary. The data were augmented by rotation, shifting, flipping, and elastic deformation [68,85].

The results of the examined segmentation methods were compared with the measures of accuracy and intersection over union (IoU). The accuracy is the percentage of correctly classified voxels, while IoU is the ratio between the intersection and the union of the obtained output U and ground truth T, i.e.,

$$\text{IoU} = \frac{|U \cap T|}{|U \cup T|}, \qquad (13)$$

thus the IoU is equal to one for perfect segmentation results, while it approaches zero for many incorrectly recognized voxels.

Finally, the segmented tomograms were refined by the guided image filtering [86]. In short, the output image u results from

$$u_q = a_x g_q + b_x \qquad \forall q \in \omega_x, \qquad (14)$$

where g is the guide image, ω_x is a square window with radius r around pixel x, and a_x and b_x are linear coefficients that are assumed to be constant within the window ω_x and can be determined by solving the minimization problem

$$E(a_x, b_x) = \frac{1}{2} \sum_{q \in \omega_x} [(a_x g_q + b_x - f_q)^2 + \epsilon a_x^2], \qquad (15)$$

where f is the input image and ϵ is a regularization parameter.

All of the pipelines described above have been implemented in Python using the PyTorch library. The resulting 3D aortic ultrastructure with collagen fibrils and PGs was visualized with the software Amira (FEI, Visualization Sciences Group).

Fig. 7. Histological sections of different layers of the aortic wall at different stretches: intima (a),(d),(g),(j), media (b),(e),(h),(k), and adventitia (c),(f),(i),(l) stained with toluidine blue at the load-free state (a)–(c) and for stretches of 1.05 (d)–(f), 1.10 (g)–(i), and 1.15 (j)–(l). The longitudinal and circumferential directions are vertical and horizontal, respectively. Scale bars denote 50 μm.

Fig. 8. Adjacent sections of the aortic media, stained with toluidine blue (a) and methylene blue-azure II-basic fuchsin (b). The longitudinal and circumferential directions are vertical and horizontal, respectively. Scale bars denote 50 μm.

Andersson [94] reported collagen stained pink to red and elastin violet, while Fritsch [95] described collagen as stained blue to purple and elastin in red. Recent studies [96,97] found that collagen and elastin were stained pink or red, which is more in line with our results (Fig. 8). The differences may be due to the use of different solvents and dilutions or post-fixation and staining of the sample prior to embedding. However, there is agreement about the light blue staining of the cytoplasm and the dark blue staining of the nucleoli.

3.3. Transmission electron microscopy

Our staining protocol resulted in a good contrast in TEM images (see Figs. 9 and 10) for both collagen fibrils and PGs. We also tested contrasting of ultra-thin sections with platinum blue, 15 min, and lead citrate, 7 min, but this procedure produced an unsatisfactory contrast (data not shown). Consequently, the subsequent steps were based on ultra-thin sections stained with uranyl acetate and lead citrate.

The montages of the ultrastructure of the tissue (see, e.g., Fig. 9) made it possible to recognize representative collagen fibril bundles, i.e. collagen fibers, before further enlargement, in order to be able to record electron tomograms of collagen fibrils together with PGs (Fig. 10). The appearance of the collagen fibers was similar to that of other vascular tissues [28,59,98], i.e. the collagen fibers were consisted of almost parallel and relatively long fibrils. Interestingly, collagen fibrils are often recognized because of their D-periodicity [16,17], which was missing in our images.

A plausible explanation of this disparity could be differences in tissue processing and staining protocols [99]. The frequently used post-fixation with osmium tetroxide [51,52], which reveals the D-periodicity of collagen, shows no PGs [100]. In addition, it has been suggested that PGs are barely visible, not because of poor staining, but because they are mostly extracted during tissue processing [101]. Similar to our study, the D-periodicity in collagen fibrils was not observed in the studies that successfully record PGs [28,59,101]. These observations speak for the explanation of different protocols, but it should be noted that the missing D-periodicity was also assigned to tissue calcifications [102], collagen damage [103] or changes in the collagen structure caused by the abdominal aortic aneurysm formation [104].
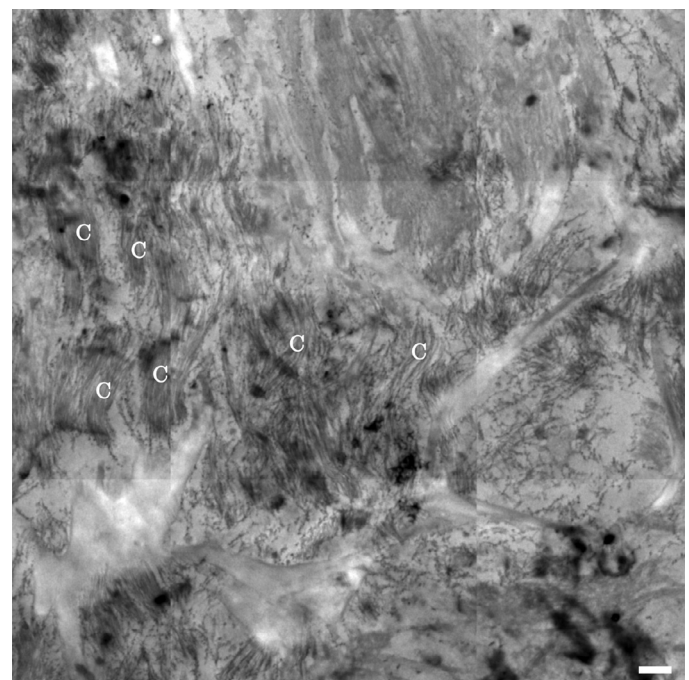
Fig. 9. Fragment of a montage of TEM images showing the ultrastructure of the aortic media at 1.15 stretch with multiple regions of collagen fibril bundles marked with C. Scale bar corresponds to 1 μm.

3.4. Segmentation

Among the tested segmentation methods, i.e. TV-ℓ_1 denoising followed by thresholding, tube detection filtering and CNNs including U-Net and ESPNet models, CNNs showed the most accurate results (Table 2). The tomograms were found to be difficult to segment because neither the collagen fibrils nor the PGs were assigned obvious gray levels. In addition, each data set showed different voxel intensities. Finally, strong irregularities in voxel intensities were observed within the structure of interest, e.g., PGs appeared darker in most images, but also contained light voxels. The TV-ℓ_1 denoising solved the irregularities in the voxel intensities,
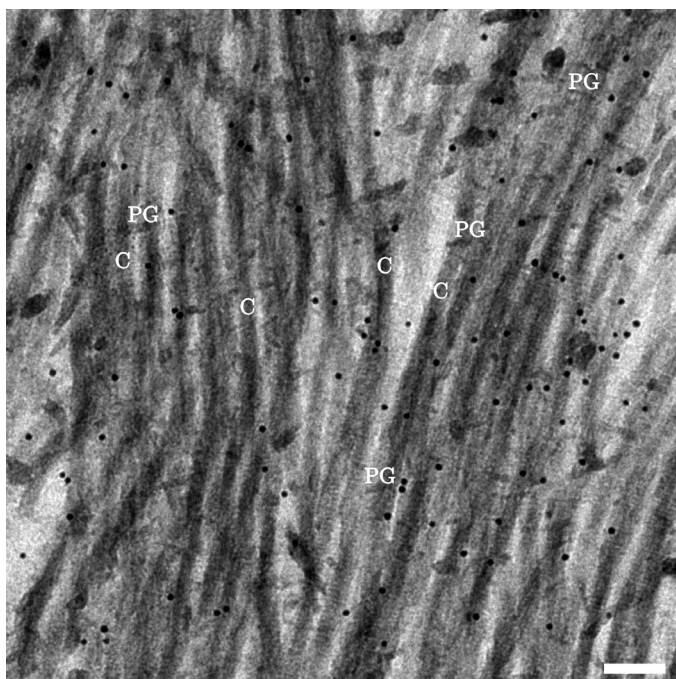
Fig. 10. The TEM image from an electron tomogram shows collagen fibrils (some labeled C) along with proteoglycans from the aortic media at a stretch of 1.15. The black dots show the protein A colloidal gold particles. Scale bar corresponds to 100 nm.

Table 2

Assessment measures, accuracy, and intersection over union (IoU), for various segmentation methods used for PGs extraction.

Segmentation method	Accuracy	IoU
Thresholding after TV-ℓ_1	0.4131	0.3018
Frangi tube detection filter	0.5227	0.2025
CNN: U-Net model	0.7279	0.5961
CNN: ESPNet model	0.9669	0.6258

but the regularization parameter λ had to be adjusted individually for each data set.

The tube detection filter was also unsuccessful for our application. Frangi et al. [73] proposed this filter for improved visualization of the human vascular system, which is imaged with magnetic resonance angiography (MRA). This filter has been widely accepted and further developed, e.g., for an application on photoacoustic images of the vasculature [105]. However, the vessels in MRA images are comparatively long, do not cross any image boundaries and, in contrast to the collagen fibrils and PGs imaged by TEM,

Table 3

Assessment measures, accuracy, and intersection over union (IoU), for CNN models used for collagen fibrils extraction.

Segmentation method	Accuracy	IoU
CNN: U-Net model	0.8269	0.7086
CNN: ESPNet model	0.9511	0.9048

take up a relatively small volume of the entire data set. In particular, collagen fibrils exceed the volume of tomograms and showed a relatively variable diameter along the axis, while PGs are relatively short. Considering that the mathematical tubularity assumption applies in the middle regions, but not at the ends, the assignment of eigenvalues is not valid for a proportionally large volume of a proteoglycan. The accuracy and IoU obtained for PGs are presented in Table 2 for the filter parameters $\alpha = 0.5$, $\beta = 0.5$, as recommended in Frangi et al. [73], and $c = 0.75$ chosen based on the value of the maximum Hessian norm [73], see Eq. (8). Both CNN models exceeded the TV-ℓ_1 denoising and the Frangi tube detection filter, as indicated in Table 2. In addition, ESPNet delivered better results in terms of accuracy and IoU for PGs (Table 2) and collagen fibrils (Table 3). Exemplary images of PGs segmented with different methods are shown in Fig. 11.

The great performance of the CNN models was mainly achieved through the data augmentation (Fig. 12). The training behavior (Figs. 13 and 14) also showed that the degree of accuracy alone was not sufficient for correct data evaluation, especially for the segmentation of PGs. Note that PGs are in a much smaller volume than collagen fibrils in the images. Thus, although the same number of images were used for PGs and collagen fibrils, less information about PGs was provided to the models. As a result, the training behavior for PGs was less smooth and even showed a local overfitting, which is indicated as spikes in the Figs. 13 and 14. In addition, it could be observed that the accuracy increased rapidly while IoU increased gradually (Fig. 14(b)). A representative 3D organization of collagen fibrils and PGs is visualized in Fig. 15. Unsurprisingly, the fine 3D organization of collagen fibrils and PGs has shown to be complex and undetectable in 2D. It can be observed that not all PGs are attached to the collagen fibrils, but that some fill the space between the fibrils with a clear distance from the collagen. In addition, some collagen fibrils, although commonly understood as being separate tubular-like structures, tend to fuse. This spatial arrangement cannot be captured and can be misinterpreted in 2D images.

4. Discussion and conclusion

The analysis of the relation between the macroscopic mechanical loading on the tissue and the nanoscopic changes of its struc-
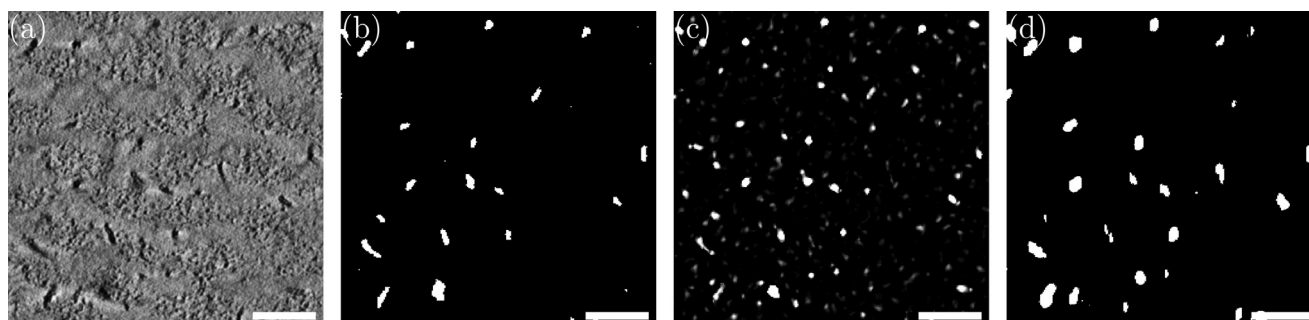

Fig. 11. Fragment of the image from a reconstructed electron tomogram (a) as well as the binarized images showing PGs segmented with different methods: the TV-ℓ_1 denoising followed by thresholding (b), the tube detection filtering (c), and the ESPNet model followed by the guided image filtering (d). Scale bars denote 100 nm.
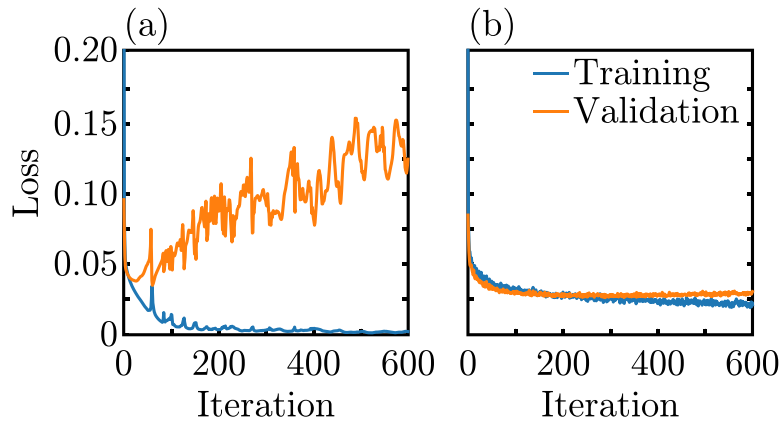
Fig. 12. Training behavior of the UNet for the segmentation of PGs shows the effects of data augmentation by comparing the loss without (a) and with (b) data augmentation, both for the training (blue) and for the validation data (orange).
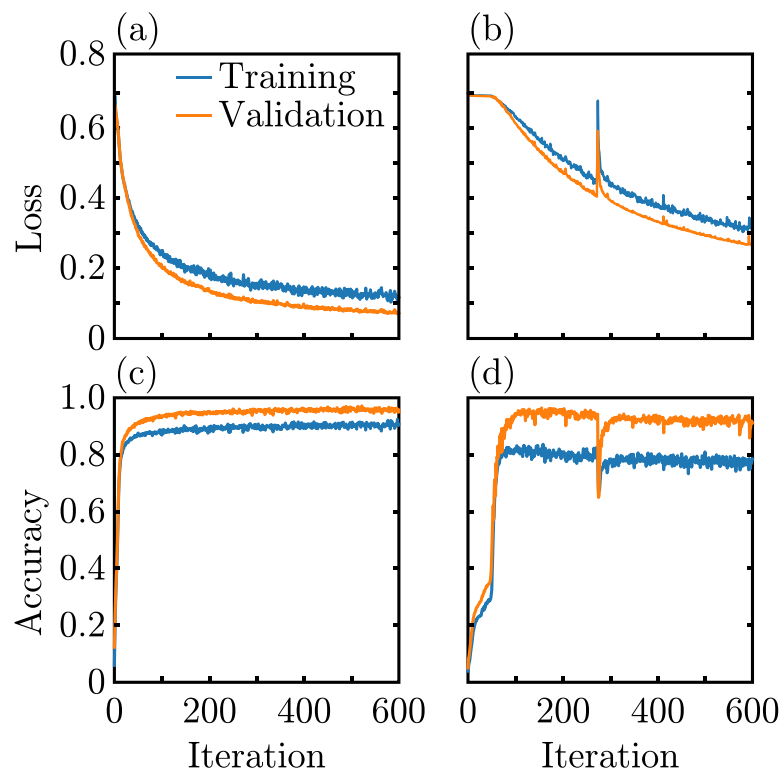
Fig. 13. Training behavior of the ESPNet for the segmentation of collagen fibrils (a),(c) and PGs (b),(d) represented by loss (a),(b) and accuracy (c),(d), both for training (blue) and for validation (orange) data.
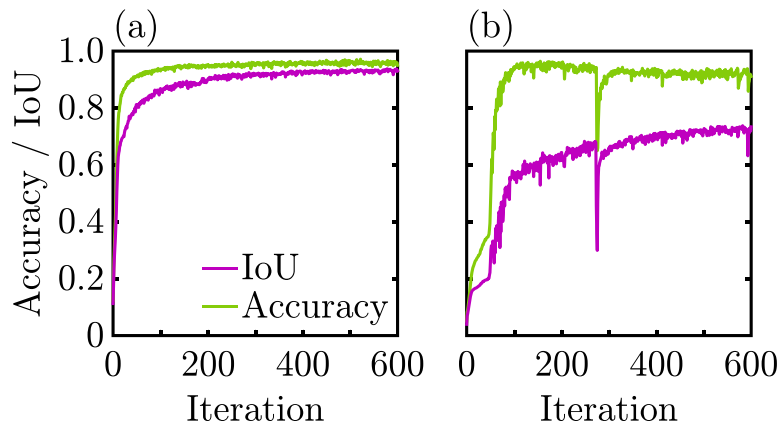
Fig. 14. The accuracy (green) and IoU (purple) of the validation data during ESPNet training for segmentation of (a) collagen fibrils and (b) PGs.
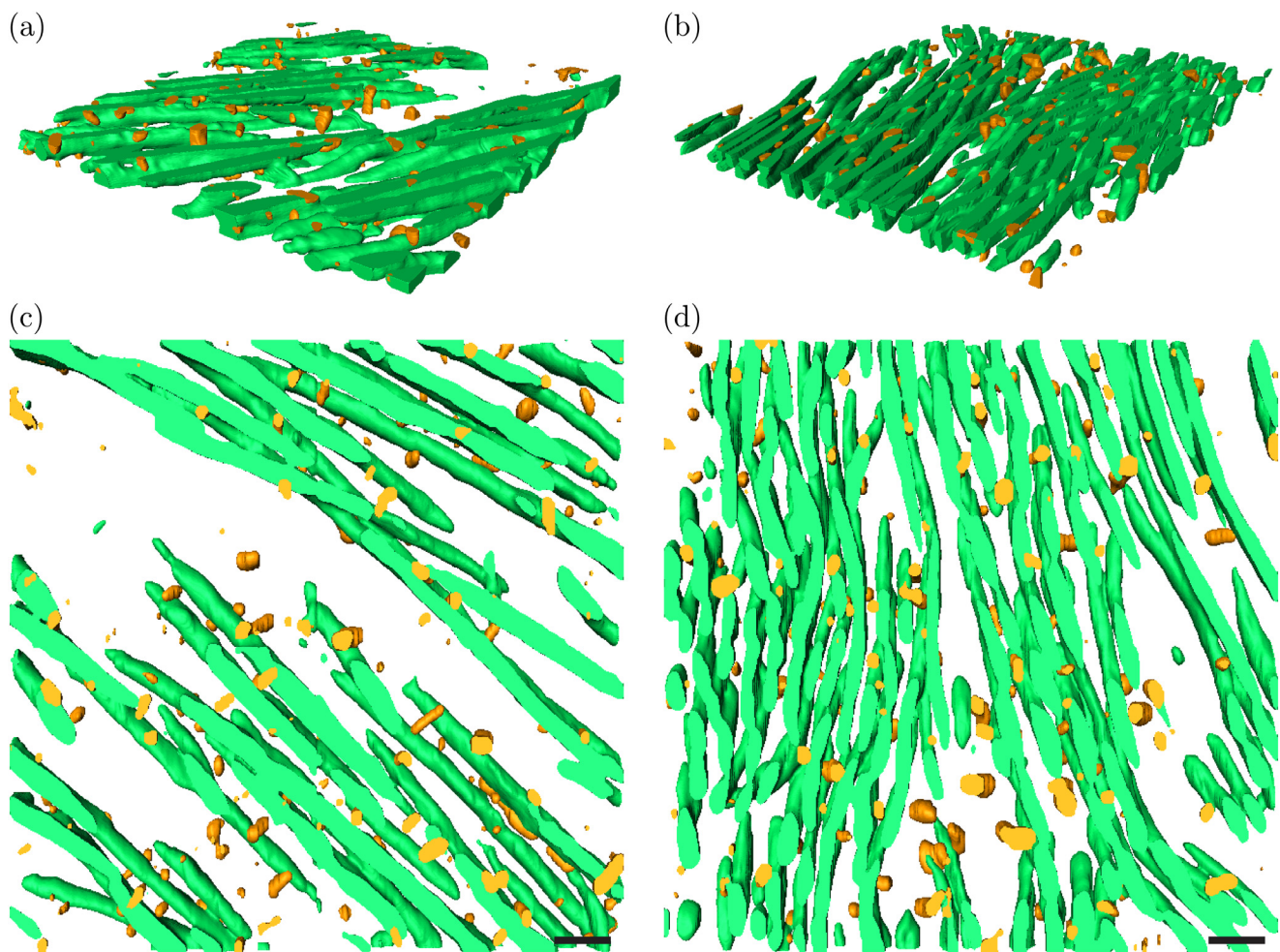
Fig. 15. Visualization of the 3D organization of collagen fibrils (green) and PGs (yellow) in the aortic media in the load-free state (a),(c) and at 1.15 stretch (b),(d) shown as axonometric projections (a),(b) and in-plane views (c),(d). Scale bars correspond to 100 nm.

ture is facing major challenges. One of these is to ensure that the structural changes observed are caused by the applied load. Therefore, in the proposed approach, we used the well-established biaxial extension test, which is often used to identify the mechanical properties of animal [25,89,106] and human aortic tissues [6,7,38,57,107–109]. In addition, we carefully designed the equibiaxial experiment taking into account the boundary conditions [54] and the uniformity of the strain field [55]. Therefore, the imaging is limited to a small area in the center of the sample. As a result, individual variability and homogeneity within an aorta cannot be recorded. Furthermore, applying this approach to highly inhomogeneous (diseased) tissues may require further validation.

The recorded mechanical response of the aortic wall (Fig. 6) agrees well with earlier studies, e.g., Haskett et al. [108] identified a greater compliance of the healthy human abdominal aorta in the circumferential direction. In addition, Niestrawska et al. [6] reported higher median Cauchy stresses in the longitudinal than in the circumferential direction for non-aneurysmal human abdominal aortas. On the other hand, Vande Geest et al. [38], [107] reported no significant difference in the mechanical response of the human abdominal aortic tissues between the longitudinal and circumferential directions. This finding was confirmed by Kamenskiy et al. [57], who tested aortas which were stiffer in either the circumferential or longitudinal direction. In summary, the mechanical behavior obtained during this study was representative of the healthy human abdominal aortic wall.

The next critical aim of this study was the precise determination of the examined location within the aortic wall. To the best of the authors' knowledge, this study presents the first guideline for the detection of aortic layers based on their in-plane architecture as stained with any staining appropriate for semi-thin resin-embedded sections. The suggested staining methods were sufficient for the layer detection, but none of them were suitable for the analysis of the structural changes of collagen fibers and therefore not comparable with second harmonic generation microscopy, as it is, e.g., in Niestrawska et al. [6].

The next goal was to image collagen fibrils including adjacent PGs. The detection of collagen fibers and fibrils is based on the available literature [28,59,101,110,111], but it should be noted that the imaging of the human media ultrastructure was previously carried out in a load-free state [28]. To the best of the authors' knowledge, this is the first study to visualize the arrangement of collagen fibrils and PGs in the stretched aortic wall. It is also worth noting that collagen fibrils are often imaged by TEM, but PGs are not. To the best of the authors' knowledge, the clear staining protocol that reveals PGs [59] has not yet been validated, e.g., by immunodetection. Although Cupromeronic Blue's compatibility with immunodetection could prove difficult, it would be of interest for future studies. Future studies could also aim to further develop our approach and visualize collagen fibrils and PGs in the aortic wall still visible in their cylindrical configuration.

The thresholding and tube detection filter proved unsuitable for our application. Moreover, the amount of data to train the CNN models was an issue, especially for PGs, as shown by the training behavior (Figs. 12–14). The manual segmentation, especially of the 3D data, is a demanding and time-consuming task [112] and introduces operator-dependent inaccuracies [113]. As a solution, the annotation of maximum intensity projections instead of 3D structures was proposed [112], but the authors found that this approach is not suitable for electron microscopy images. In this context, we have tested the data augmentation approach and proven it sucessful. Although our segmentation approach excludes the subjectivity of different operators, it is still based on the operator-depended training data provided. It should therefore be noted that the boundary of the segmented objects could be influenced by a bias caused by the operator. It is noteworthy that the boundaries are critical when analyzing the contact between the segmented objects.

Although our study aimed to develop an effective approach and was limited to only one aorta, we were able to observe some ultrastructural changes in the arrangement of collagen fibrils and PGs with increased degrees of stretch. These preliminary observations might suggest that collagen fibrils are more densely packed at higher stretches and that PGs appear to be reoriented towards the radial direction, i.e., out-of-plane.

The results obtained and the proposed protocols open up various possibilities. The geometry of binarized objects representing collagen fibrils and PGs could be quantified. As future work, it is planned to analyze the segmented collagen fibrils and PGs with regard to the orientation, e.g., using the eigenvectors [73], and the diameter, e.g., with the help of the adaptive multiscale medialness function [114] or the distance transform [115,116]. These quantifications would enable a comparison of the organization of collagen fibrils and PGs in the load-free and loaded states and prove (or disprove) their contribution to the macroscopic deformation of the tissue. For example, on the one hand, the increased length and reduced diameter of PGs could support the hypothesis of their function as elastic bridges. The separation of PGs from collagen fibrils under increased loading could support the hypothesis of their role as a mechanical coupling. On the other hand, little or no geometric changes could indicate no contribution to load transmission. The comparison of the ultrastructure of collagen fibers in health and disease would deepen our understanding of the relationship between the architecture of collagen fibrils and aortic diseases. In addition, such a knowledge is essential for the improvement and development of constitutive [1,2] and multiscale [117–119] material models of soft biological tissues. Furthermore, the knowledge of the relationship between the structure and the mechanical properties of the ECM is essential for the development of suitable scaffolds for tissue engineering [120,121].

Declaration of Competing Interest

The authors declare that they have no known competing financial interests or personal relationships that could have appeared to influence the work reported in this paper.

Acknowledgements

References

[1] G.A. Holzapfel, J.A. Niestrawska, R.W. Ogden, A.J. Reinisch, A.J. Schriefl, Modelling non-symmetric collagen fibre dispersion in arterial walls, J. R. Soc. Interface 12 (2015) 20150188.

[2] K. Li, R.W. Ogden, G.A. Holzapfel, A discrete fibre dispersion method for excluding fibres under compression in the modelling of fibrous tissues, J. R. Soc. Interface 15 (2018) 20170766.

[3] S. Cranford, M.J. Buehler, Materiomics: biological protein materials, from nano to macro, Nanotechnol. Sci. Appl. 3 (2010) 127–148.

[4] H. Weisbecker, C. Viertler, D.M. Pierce, G.A. Holzapfel, The role of elastin and collagen in the softening behavior of the human thoracic aortic media, J. Biomech. 46 (2013) 1859–1865.

[5] A.J. Schriefl, T. Schmidt, D. Balzani, G. Sommer, G.A. Holzapfel, Selective enzymatic removal of elastin and collagen from human abdominal aortas: uniaxial mechanical response and constitutive modeling, Acta Biomater. 17 (2015) 125–136.

[6] J.A. Niestrawska, C. Viertler, P. Regitnig, T.U. Cohnert, G. Sommer, G.A. Holzapfel, Microstructure and mechanics of healthy and aneurysmatic abdominal aortas: experimental analysis and modeling, J. R. Soc. Interface 13 (2016) 20160620.

[7] J.A. Niestrawska, P. Regitnig, C. Viertler, T.U. Cohnert, A.R. Babu, G.A. Holzapfel, The role of tissue remodeling in mechanics and pathogenesis of abdominal aortic aneurysms, Acta Biomater. 88 (2019) 149–161.

[8] R. Rezakhaniha, A. Agianniotis, J.T.C. Schrauwen, A. Griffa, D. Sage, C.V.C. Bouten, F.N. van de Vosse, M. Unser, N. Stergiopulos, Experimental investigation of collagen waviness and orientation in the arterial adventitia using confocal laser scanning microscopy, Biomech. Model. Mechanobiol. 11 (2012) 461–473.

[9] S. Zeinali-Davarani, Y. Wang, M.J. Chow, R. Turcotte, Y. Zhang, Contribution of collagen fiber undulation to regional biomechanical properties along porcine thoracic aorta, J. Biomech. Eng. 137 (2015) 051001.

[10] G.A. Holzapfel, R.W. Ogden, Biomechanical relevance of the microstructure in artery walls with a focus on passive and active components, Am. J. Physiol. Heart Circ. Physiol. 315 (2018) H540–H549.

[11] G.A. Holzapfel, Collagen in arterial walls: biomechanical aspects, in: P. Fratzl (Ed.), Collagen. Structure and Mechanics, Springer-Verlag, Heidelberg, 2008, pp. 285–324.

[12] K.G. McCullagh, V.C. Duance, K.A. Bishop, The distribution of collagen types I, III and V (AB) in normal and atherosclerotic human aorta, J. Pathol. 130 (1980) 45–55.

[13] K. Murata, T. Motayama, C. Kotake, Collagen types in various layers of the human aorta and their changes with the atherosclerotic process, Atherosclerosis 60 (1986) 251–262.

[14] E. Maurel, C.A. Shuttleworth, H. Bouissou, Interstitial collagens and ageing in human aorta, Virchows Arch. A 410 (1987) 383–390.

[15] D.J.S. Hulmes, Collagen diversity, synthesis and assembly, in: P. Fratzl (Ed.), Collagen: Structure and Mechanics, Springer, 2008, pp. 15–47.

[16] T.J. Wess, Collagen fibrillar structure and hierarchies, in: P. Fratzl (Ed.), Collagen: Structure and Mechanics, Springer, 2008, pp. 49–80.

[17] M.D. Shoulders, R.T. Raines, Collagen structure and stability, Annu. Rev. Biochem. 78 (2009) 929–958.

[18] Y.L. Sun, Z.P. Luo, A. Fertala, K.A. An, Direct quantification of the flexibility of type I collagen monomer, Biochem. Biophys. Res. Commun. 295 (2002) 382–386.

[19] P. Dutov, O. Antipova, S. Varma, J.P.R.O. Orgel, J.D. Schieber, Measurement of elastic modulus of collagen type I single fiber, PLoS ONE 11 (2016) e0145711.

[20] H. Wolinsky, S. Glagov, Structural basis for the static mechanical properties of the aortic media, Circ. Res. 14 (1964) 400–413.

[21] H. Chen, M.N. Slipchenko, Y. Liu, X. Zhao, J.-X. Cheng, Y. Lanir, G.S. Kassab, Biaxial deformation of collagen and elastin fibers in coronary adventitia, J. Appl. Physiol. 115 (2013) 1683–1693.

[22] M.-J. Chow, R. Turcotte, C.P. Lin, Y. Zhang, Arterial extracellular matrix: a mechanobiological study of the contributions and interactions of elastin and collagen, Biophys. J. 106 (2014) 2684–2692.

[23] C. Cavinato, C. Helfenstein-Didier, T. Olivier, S.R.d. Roscoat, N. Laroche, P. Badel, Biaxial loading of arterial tissues with 3D in situ observations of adventitia fibrous microstructure: a method coupling multi-photon confocal microscopy and bulge inflation test, J. Mech. Behav. Biomed. Mater. 74 (2017) 488–498.

[24] S. Sugita, T. Matsumoto, Multiphoton microscopy observations of 3D elastin and collagen fiber microstructure changes during pressurization in aortic media, Biomech. Model. Mechanobiol. 16 (2017) 763–773.

[25] H. Li, J.M. Mattson, Y. Zhang, Integrating structural heterogeneity, fiber orientation, and recruitment in multiscale ECM mechanics, J. Mech. Behav. Biomed. Mater. 92 (2019) 1–10.

[26] A.G. Vouyouka, B.J. Pfeiffer, T.K. Liem, T.A. Taylor, J. Mudaliar, C.L. Phillips, The role of type I collagen in aortic wall strength with a homotrimeric $[\alpha 1(I)]_3$ collagen mouse model, J. Vasc. Surg. 33 (2001) 1263–1270.

[27] J.H. Lindeman, B.A. Ashcroft, J.W. Beenakker, M. van Es, N.B. Koekkoek, F.A. Prins, J.F. Tielemans, H. Abdul-Hussien, R.A. Bank, T.H. Oosterkamp, Dis-

tinct defects in collagen microarchitecture underlie vessel-wall failure in advanced abdominal aneurysms and aneurysms in Marfan syndrome, Proc. Natl. Acad. Sci. USA 107 (2010) 862–865.

[28] K.P. Dingemans, P. Teeling, J.H. Lagendijk, A.E. Becker, Extracellular matrix of the human aortic media: an ultrastructural histochemical and immunohistochemical study of the adult aortic media, Anat. Rec. 258 (2000) 1–14.

[29] L. Schaefer, R.M. Schaefer, Proteoglycans: from structural compounds to signaling molecules, Connect. Tissue Res. 339 (2010) 237–246.

[30] J.R. Couchman, C.A. Pataki, An introduction to proteoglycans and their localization, J. Histochem. Cytochem. 60 (2012) 885–897.

[31] C.M. Kelleher, S.E. McLean, R.P. Mecham, Vascular extracellular matrix and aortic development, Curr. Top. Dev. Biol. 62 (2004) 153–188.

[32] J.E. Wagenseil, R.P. Mecham, Vascular extracellular matrix and arterial mechanics, Physiol. Rev. 89 (2009) 957–989.

[33] S. Sherifova, G.A. Holzapfel, Biochemomechanics of the thoracic aorta in health and disease, Prog. Biomed. Eng. 2 (2020) 032002.

[34] W. Völker, A. Schmidt, E. Buddecke, Cytochemical changes in a human arterial proteoglycan related to atherosclerosis, Atherosclerosis 77 (1989) 117–130.

[35] T.N. Wight, A role for proteoglycans in vascular disease, Matrix Biol. 71-72 (2018) 396–420.

[36] F. Tanios, M.W. Gee, J. Pelisek, S. Kehl, J. Biehler, V. Grabher-Meier, W.A. Wall, H.H. Eckstein, C. Reeps, Interaction of biomechanics with extracellular matrix components in abdominal aortic aneurysm wall, Eur. J. Vasc. Endovasc. Surg. 50 (2015) 167–174.

[37] G.A. Holzapfel, G. Sommer, P. Regitnig, Anisotropic mechanical properties of tissue components in human atherosclerotic plaques, J. Biomech. Eng. 126 (2004) 657–665.

[38] J.P. Vande Geest, M.S. Sacks, D.A. Vorp, The effects of aneurysm on the biaxial mechanical behavior of human abdominal aorta, J. Biomech. 39 (2006) 1324–1334.

[39] K. Linka, V.N. Khiêm, M. Itskov, Multi-scale modeling of soft fibrous tissues based on proteoglycan mechanics, J. Biomech. 49 (2016) 2349–2357.

[40] J.E. Scott, Elasticity in extracellular matrix 'shape modules' of tendon, cartilage, etc. a sliding proteoglycan-filament model, J. Physiol. 553 (2003) 335–343.

[41] P.S. Robinson, T. Huang, E. Kazam, R.V. Iozzo, D.E. Birk, L.J. Soslowsky, Influence of decorin and biglycan on mechanical properties of multiple tendons in knockout mice, J. Biomech. Eng. 127 (2005) 181–185.

[42] S. Vesentini, A. Redaelli, F.M. Montevecchi, Estimation of the binding force of the collagen molecule-decorin core protein complex in collagen fibril, J. Biomech. 38 (2005) 433–443.

[43] S. Rigozzi, R. Müller, A. Stemmer, J.G. Snedeker, Tendon glycosaminoglycan proteoglycan sidechains promote collagen fibril sliding – AFM observations at the nanoscale, J. Biomech. 46 (2013) 813–818.

[44] G. Fessel, J.G. Snedeker, Evidence against proteoglycan mediated collagen fibril load transmission and dynamic viscoelasticity in tendon, Matrix Biol. 28 (2009) 503–510.

[45] F.S.A. Cavalcante, S. Ito, K. Brewer, H. Sakai, A.M. Alencar, M.P. Almeida, J.S. Andrade, A. Majumdar, E.P. Ingenito, B. Suki, Mechanical interactions between collagen and proteoglycans: implications for the stability of lung tissue, J. Appl. Physiol. 98 (2005) 672–679.

[46] Y. Lanir, Biorheology and flux in swelling tissue. I. Biocomponent theory for small deformation including concentration effect, Biorheology 24 (1987) 173–187.

[47] E.U. Azeloglu, M.B. Albro, V.A. Thimmappa, G.A. Ateshian, K.D. Costa, Heterogeneous transmural proteoglycan distribution provides a mechanism for regulating residual stresses in the aorta, Am. J. Physiol. Heart Circ. Physiol. 294 (2008) H1197–1205.

[48] J.M. Mattson, R. Turcotte, Y. Zhang, Glycosaminoglycans contribute to extracellular matrix fiber recruitment and arterial wall mechanics, Biomech. Model. Mechanobiol. 16 (2017) 213–225.

[49] R.G. Haverkamp, M.A. Williams, J.E. Scott, Stretching single molecules of connective tissue glycans to characterize their shape-maintaining elasticity, Biomacromolecules 6 (2005) 1816–1818.

[50] S. Subramaniam, P. Zhang, J. Lefman, J. Juliani, K. M, Electron tomography: a powerful tool for 3D cellular microscopy, ASM News 69 (2003) 240–245.

[51] N. Cortadellas, A. Garcia, E. Fernández, Transmission electron microscopy in cell biology: sample preparation techniques and image information, in: J.R. Seoane (Ed.), Handbook of Instrumental Techniques, CCiTUB, Barcelona, 2010.

[52] M. Winey, J.B. Meehl, E.T. O'Toole, J. T. H. Giddings, Conventional transmission electron microscopy, Mol. Biol. Cell 25 (2014) 319–323.

[53] G. Sommer, T.C. Gasser, P. Regitnig, M. Auer, G.A. Holzapfel, Dissection properties of the human aortic media: an experimental study, J. Biomech. Eng. 130 (2008) 021007–1–12.

[54] W. Sun, M.S. Sacks, M.J. Scott, Effects of boundary conditions on the estimation of the planar biaxial mechanical properties of soft tissues, J. Biomech. Eng. 127 (2005) 709–715.

[55] A. Eilaghi, J.G. Flanagan, G.W. Brodland, C.R. Ethier, Strain uniformity in biaxial specimens is highly sensitive to attachment details, J. Biomech. Eng. 131 (2009) 0910031–0910037.

[56] G. Sommer, D.C. Haspinger, M. Andrä, M. Sacherer, C. Viertler, P. Regitnig, G.A. Holzapfel, Quantification of shear deformations and corresponding stresses in the biaxially tested human myocardium, Ann. Biomed. Eng. 43 (2015) 2234–2348.

[57] A.V. Kamenskiy, Y.A. Dzenis, S.A. Kazmni, M.A. Pemberton, I.I. Pipinos, N.Y. Phillips, K. Herber, T. Woodford, R.E. Bowen, C.S. Lomneth, J.N. MacTaggart, Biaxial mechanical properties of the human thoracic and abdominal aorta, common carotid, subclavian, renal and common iliac arteries, Biomech. Model. Mechanobiol. 13 (2014) 1341–1359.

[58] J.D. Humphrey, R.K. Strumpf, F.C.P. Yin, Biaxial mechanical behavior of excised ventricular epicardium, Am. J. Physiol. Heart Circ. Physiol. 259 (1990) H101–H108.

[59] C. Williams, J. Liao, E.M. Joyce, B. Wang, J.B. Leach, M.S. Sacks, J.Y. Wong, Altered structural and mechanical properties in decellularized rabbit carotid arteries, Acta Biomater. 5 (2009) 993–1005.

[60] A. Wittgenstein, Ultrastructural investigation of biaxially loaded human aortic tissue, Master's thesis, 2018, Biomedical Engineering, Graz University of Technology

[61] P. Böck (Ed.), Der Semidünnschnitt, J. F. Bergmann Verlag, München, Germany, 1984.

[62] G. Leitinger, S. Masich, J. Neumüller, M.A. Pabst, M. Pavelka, F.C. Rind, O. Shupliakov, P.J. Simmons, D. Kolb, Structural organization of the presynaptic density at identified synapses in the locust central nervous system, J. Comp. Neurol. 520 (2012) 384–400.

[63] D. Serwas, A. Dammermann, Ultrastructural analysis of Caenorhabditis elegans cilia, Methods Cell Biol. 129 (2015) 341–367.

[64] D. Kolb, E. Pritz, B. Steinecker-Frohnwieser, B. Lohberger, A. Deutsch, T. Kroneis, A. El-Heliebi, G. Dohr, K. Meditz, K. Wagner, H. Koefeler, G. Leitinger, A. Leithner, B. Liegl-Atzwanger, D. Zweytick, B. Rinner, Extended ultrastructural characterization of chordoma cells: the link to new therapeutic options, PLoS ONE 9 (2014) e114251.

[65] D.N. Mastronarde, Automated electron microscope tomography using robust prediction of specimen movements, J. Struct. Biol. 152 (2005) 31–51.

[66] J.R. Kremer, D.N. Mastronarde, J.R. McIntosh, Computer visualization of three-dimensional image data using IMOD, J. Struct. Biol. 116 (1996) 71–76.

[67] J. Schindelin, I. Arganda-Carreras, E. Frise, V. Kaynig, M. Longair, T. Pietzsch, S. Preibisch, C. Rueden, S. Saalfeld, B. Schmid, J.Y. Tinevez, D.J. White, V. Hartenstein, K. Eliceiri, P. Tomancak, A. Cardona, Fiji: an open-source platform for biological-image analysis, Nat. Methods 9 (2012) 676–682.

[68] S.A. Schneider, Segmentation of collagen fibrils and proteoglycans from reconstructed tilt series acquired by TEM, 2020, Master's thesis, Biomedical Engineering, Graz University of Technology

[69] V. Horak, K. Bredies, A two-stage classifier for collagen in electron tomography images using a convolutional neural network and TV segmentation, in: P.M. Roth, A. Pichler, R. Sablatnig, G.G. Stübl, M. Vincze (Eds.), Proceedings of ARW & OAGM Workshop 2019, Verlag der Technischen Universität Graz, Steyr, 2019, pp. 209–210.

[70] J. Wu, Introduction to convolutional neural networks, Natl. Key Lab Novel Softw. Technol., Nanjing University, China, 2017.

[71] F. Emmert-Streib, Z. Yang, H. Feng, S. Tripathi, M. Dehmer, An introductory review of deep learning for prediction models with big data, Front. Artif. Intell. 3 (2020) 4.

[72] A. Chambolle, T. Pock, An introduction to continuous optimization for imaging, Acta Numer. 25 (2016) 161–319.

[73] A.F. Frangi, W.J. Niessen, K.L. Vincken, M.A. Viergever, Multiscale vessel enhancement filtering, in: W. Wells, A. Colchester, S. Delp (Eds.), Medical Image Computing and Computer-Assisted Intervention – MICCAI '98, Lecture Notes in Computer Science, vol. 1496, Springer, Berlin, Heidelberg, 1998, pp. 130–137.

[74] O. Ronneberger, P. Fischer, T. Brox, U-Net convolutional networks for biomedical image segmentation, in: N. Navab, J. Hornegger, W. Wells, A. Frangi (Eds.), Medical Image Computing and Computer-Assisted Intervention – MICCAI 2015, Lecture Notes in Computer Science, volume 9351, Springer, Cham, Heidelberg, New York, Dordrecht, London, 2015, pp. 234–241.

[75] S. Mehta, M. Rastegari, A. Caspi, L. Shapiro, H. Hajishirzi, ESPNet: efficient spatial pyramid of dilated convolutions for semantic segmentation, in: V. Ferrari, M. Hebert, C. Sminchisescu, Y. Weiss (Eds.), Computer Vision – ECCV 2018, Lecture Notes in Computer Science, vol. 11214, Springer, Cham, 2018, pp. 561–580.

[76] L.I. Rudin, S. Osher, E. Fatemi, Nonlinear total variation based noise removal algorithms, Physica D 60 (1992) 259–268.

[77] T. Lindeberg, Scale-space theory: a basic tool for analysing structures at different scales, J. Appl. Stat. 21 (1994) 225–270.

[78] C.E. Nwankpa, W. Ijomah, A. Gachagan, S. Marshall, Activation functions: comparison of trends in practice and research for deep learning, in: Proceedings of the 2nd International Conference on Computational Sciences and Technology, MUET, Jamshoro, 2020, pp. 124–133.

[79] K. Janocha, W.M. Czarnecki, On loss functions for deep neural networks in classification, Schedae Informaticae 25 (2016) 49–59.

[80] D.P. Kingma, J.L. Ba, Adam: a method for stochastic optimization, in: Y. Bengio, Y. LeCun (Eds.), Proceedings of the 3rd International Conference on Learning Representations, ICLR, San Diego, 2015.

[81] S. Ruder, An overview of gradient descent optimization algorithms, (2016) arXiv preprint arXiv:1609.04747.

[82] D. Ulyanov, A. Vedaldi, V. Lempitsky, Instance normalization: the missing ingredient for fast stylization, (2016) arXiv preprint arXiv:1607.08022.

[83] Y. Wu, K. He, Group normalization, Int. J. Comput. Vision 128 (2020) 742–755.

[84] P. Knöbelreiter, C. Sormann, A. Shekhovtsov, F. Fraundorfer, T. Pock, Belief propagation reloaded: learning BP-layers for labeling problems, in:

L. O'Conner (Ed.), Proceedings of the 2020 IEEE/CVF Conference on Computer Vision and Pattern Recognition, IEEE, Los Alamitos, California, Washington, Tokyo, 2020, pp. 7897–7906.

[85] P.Y. Simard, D. Steinkraus, J.C. Platt, Best practices for convolutional neural networks applied to visual document analysis, in: B. Werner (Ed.), Proceedings of the Seventh International Conference on Document Analysis and Recognition, IEEE, Los Alamitos, California, Washington, Brussels, Tokyo, 2003, pp. 958–963.

[86] K. He, J. Sun, X. Tang, Guided image filtering, IEEE Trans. Pattern Anal. Mach. Intell. 35 (2013) 1397–1409.

[87] G.A. Holzapfel, G. Sommer, C.T. Gasser, P. Regitnig, Determination of layer-specific mechanical properties of human coronary arteries with non-atherosclerotic intimal thickening, and related constitutive modeling, Am. J. Physiol. Heart Circ. Physiol. 289 (2005) H2048–2058.

[88] H. Weisbecker, D.M. Pierce, P. Regitnig, G.A. Holzapfel, Layer-specific damage experiments and modeling of human thoracic and abdominal aortas with non-atherosclerotic intimal thickening, J. Mech. Behav. Biomed. Mater. 12 (2012) 93–106.

[89] J.A. Peña, V. Corral, M.A. Martínez, E. Peña, Over length quantification of the multiaxial mechanical properties of the ascending, descending and abdominal aorta using digital image correlation, J. Mech. Behav. Biomed. Mater. 77 (2018) 434–445.

[90] G.A. Holzapfel, T.C. Gasser, R.W. Ogden, A new constitutive framework for arterial wall mechanics and a comparative study of material models, J. Elasticity 61 (2000) 1–48.

[91] G. Sridharan, A. Shankar, Toluidine blue: A review of its chemistry and clinical utility, J. Oral Maxillofac Pathol. 16 (2012) 251–255.

[92] B.C. Vidal, M.L.S. Mello, Toluidine blue staining for cell and tissue biology applications, Acta Histochem. 121 (2019) 101–112.

[93] M.K. O'Connell, S. Murthy, S. Phan, C. Xu, J. Buchanan, R. Spilker, R.L. Dalman, C.K. Zarins, W. Denk, C.A. Taylor, The three–dimensional micro– and nanostructure of the aortic medial lamellar unit measured using 3D confocal and electron microscopy imaging, Matrix Biol. 27 (2008) 171–181.

[94] M. Andersson, Stains for plastic embedded tissue sections. II. Staining of sections from different animal, human and plant tissues with a methylene blue-azure II - basic fuchsin stain, LKB-Produkter AB AN 303, 1977.

[95] H. Fritsch, Staining of different tissues in thick epoxy resin-impregnated sections of human fetuses, Biotech. Histochem. 64 (1989) 77–79.

[96] F. D'Amico, A polychromatic staining method for epoxy embedded tissue: a new combination of methylene blue and basic fuchsine for light microscopy, Biotech. Histochem. 80 (2005) 207–210.

[97] S. Morikawa, A. Sato, T. Ezaki, A simple, one-step polychromatic staining method for epoxy-embedded semithin tissue sections, Microscopy (Oxf) 67 (2018) 331–344.

[98] M.A. Wali, R.A. Eid, Changes of elastic and collagen fibers in varicose veins, Int. Angiol. 21 (2002) 337–343.

[99] K.E. Kadler, D.F. Holmes, J.A. Trotter, J.A. Chapman, Collagen fibril formation, Biochem. J. 316 (1996) 1–11.

[100] J.E. Scott, Collagen-proteoglycan interactions. Localization of proteoglycans in tendon by electron microscopy, Biochem. J. 187 (1980) 887–891.

[101] K.P. Dingemans, M.A.V.d.B. Weerman, Rapid contrasting of extracellular elements in thin sections, Ultrastruct. Pathol. 14 (1990) 519–527.

[102] F. Ortolani, F. Tubaro, L. Petrelli, A. Gandaglia, M. Spina, M. Marchini, Copper retention, calcium release and ultrastructural evidence indicate specific Cuprolinic Blue uptake and peculiar modifications in mineralizing aortic valves, Histochem. J. 34 (2002) 41–50.

[103] J.L. Zitnay, Y. Li, Z. Qin, B.H. San, B. Depalle, S.P. Reese, M.J. Buehler, S.M. Yu, J.A. Weiss, Molecular level detection and localization of mechanical damage in collagen enabled by collagen hybridizing peptides, Nat. Commun. 8 (2017) 14913.

[104] B. Jones, J.R. Tonniges, A. Debski, B. Albert, D.A. Yeung, N. Gadde, A. Mahajan, N. Sharma, E.P. Calomeni, M.R. Go, C.P. Hans, G. Agarwal, Collagen fibril abnormalities in human and mice abdominal aortic aneurysm, Acta Biomater. 110 (2020) 129–140.

[105] T. Oruganti, J.G. Laufer, B.E. Treeby, Vessel filtering of photoacoustic images, Proc. SPIE 8581 (2013) 85811W.

[106] J.A. Peña, M.A. Martínez, E. Peña, Layer-specific residual deformations and uniaxial and biaxial mechanical properties of thoracic porcine aorta, J. Mech. Behav. Biomed. Mater. 50 (2015) 55–69.

[107] J.P. Vande Geest, M.S. Sacks, D.A. Vorp, Age dependency of the biaxial biomechanical behavior of human abdominal aorta, J. Biomech. Eng. 126 (2004) 815–822.

[108] D. Haskett, G. Johnson, A. Zhou, U. Utzinger, J. Vande Geest, Microstructural and biomechanical alterations of the human aorta as a function of age and location, Biomech. Model. Mechanobiol. 9 (2010) 725–736.

[109] M. Di Giuseppe, G. Alotta, V. Agnese, D. Bellavia, G.M. Raffa, V. Vetri, M. Zingales, S. Pasta, M. Pilato, Identification of circumferential regional heterogeneity of ascending thoracic aneurysmal aorta by biaxial mechanical testing, J. Mol. Cell Cardiol. 130 (2019) 205–215.

[110] G.S. Montes, Structural biology of the fibres of the collagenous and elastic systems, Cell Biol. Int. 20 (1996) 15–27.

[111] M. Raspanti, T. Congiu, A. Alessandrini, P. Gobbi, A. Ruggeri, Different patterns of collagen-proteoglycan interaction: a scanning electron microscopy and atomic force microscopy study, Eur. J. Histochem. 44 (2000) 335–343.

[112] M. Koziński, A. Mosinska, M. Salzmann, P. Fua, Tracing in 2D to reduce the annotation effort for 3D deep delineation of linear structures, Med. Image Anal. 60 (2020) 101590.

[113] E. Huotilainen, R. Jaanimets, J. Valášek, P. Marcián, M. Salmi, J. Tuomi, A. Mäkitie, J. Wolff, Inaccuracies in additive manufactured medical skull models caused by the DICOM to STL conversion process, J. Craniomaxillofac. Surg. 42 (2014) 259–265.

[114] T. Pock, R. Beichel, H. Bischof, A novel robust tube detection filter for 3D centerline extraction, in: H. Kalviainen, J. Parkkinen, A. Kaarna (Eds.), Image Analysis. SCIA 2005, Lecture Notes in Computer Science, vol. 3540, Springer, Berlin, Heidelberg, 2005, pp. 481–490.

[115] G. Borgefors, Distance transformations in digital images, Comput. Vis. Graph. Image Process. 34 (1986) 344–371.

[116] J. Wu, B. Rajwa, D.L. Filmer, C.M. Hoffmann, B. Yuan, C.S. Chiang, J. Sturgis, J.P. Robinson, Analysis of orientations of collagen fibers by novel fiber-tracking software, Microsc. Microanal. 9 (2003) 574–580.

[117] H.N. Hayenga, B.C. Thorne, S.M. Peirce, J.D. Humphrey, Ensuring congruency in multiscale modeling: towards linking agent based and continuum biomechanical models of arterial adaptation, Ann. Biomed. Eng. 39 (2011) 2669–2682.

[118] J.R. Thunes, J.A. Phillippi, T.G. Gleason, D.A. Vorp, S. Maiti, Structural modeling reveals microstructure-strength relationship for human ascending thoracic aorta, J. Biomech. 71 (2018) 84–93.

[119] M. Dalbosco, T.A. Carniel, E.A. Fancello, G.A. Holzapfel, Multiscale numerical analyses of arterial tissue with embedded elements in the finite strain regime, Comput. Methods in Appl. Mech. Engrg 381 (2021) 113844.

[120] A. Brightman, B.P. Rajwa, J.E. Sturgis, M.E. McCallister, J.P. Robinson, S.L. Voytik-Harbin, Time-lapse confocal reflection microcopy of collagen fibrillogenesis and extracellular matrix assembly in vitro, Biopolymers 54 (2000) 222–234.

[121] F. Opitz, K. Schenke-Layland, T.U. Cohnert, B. Starcher, K.J. Halbhuber, D.P. Martin, U.A. Stock, Tissue engineering of aortic tissue: Dire consequence of suboptimal elastic fiber synthesis in vivo, Cardiovasc. Res. 63 (2004) 719–730.